Journal of Hydrology 612 (2022) 128221

Contents lists available at ScienceDirect

Journal of Hydrology

journal homepage: www.elsevier.com/locate/jhydrol

Research papers

Impact dynamics of mud flows against rigid walls

Cristiana Di Cristo [a], Oreste Fecarotta [a], Michele Iervolino [b], Andrea Vacca [a,*]

[a] Dipartimento di Ingegneria Civile, Edile ed Ambientale, Università degli Studi di Napoli "Federico II", Via Claudio 21, 80125 Napoli, Italy
[b] Dipartimento di Ingegneria, Università degli Studi della Campania "Luigi Vanvitelli", Via Roma 29, 81031 Aversa, CE, Italy

ARTICLE INFO

This manuscript was handled by Marco Borga, Editor-in-Chief, with the assistance of Francesco Comiti, Associate Editor

Keywords:
Mud flow
Power-law rheology
Shear-thinning fluid
Dam break
Impact force

ABSTRACT

Mud flows represent one of the major causes of natural hazards in mountain regions. Similarly to debris flows, they consist of a hyper-concentrated mixture of water and sediments flowing down a slope and may cause serious damages to people and structures. The present paper investigates the force produced by a dam-break wave of mud impacting against a rigid wall. A power-law shear-thinning model is used to describe the rheology of the hyper-concentrated mixture. A one-dimensional shallow water model is adopted and a second-order Finite Volume scheme is employed to numerically solve the governing equations. The results indicate that depending on the fluid rheological parameters and on the bottom slope, there exists a minimum value of the wall distance above which the peak force does not exceed the asymptotic value of the hydrostatic final condition. For two different values of the channel slope, the dimensionless value of this lower bound is individuated for several values of the power-law exponent and of a dimensionless Basal Drag coefficient. An estimation of the maximum peak force for wall distance smaller than the minimum value is also provided.

1. Introduction

Mud flows are among the major forms of natural hazards in many areas all over the world and they may be extreme events in some conditions. Similarly to debris flows, they involve a water–sediment mixture moving under the effect gravity under proper geomorphological conditions, usually triggered by either short heavy rainfalls or long periods of rain. These flows are often distinguished based on the quantity and the characteristics of the solid fraction (Takahashi, 2018) and generally mud-flows correspond to highly-concentrated mixtures of water and fine sediments, in which volumetric solid concentration varies from 6 to 60 % (Ng and Mei, 1994; O'Brien, 2003; Widjaja and Hsien-Heng Lee, 2013).

Along with debris and mud flows, lava flows, characterized by a mass of volcanic material flowing over natural slopes due to the gravity, may also be regarded as dangerous and sudden events (Harris, 2015).

Debris, mud and lava flows can also be related to quite high hazard due to the impossibility to predict the triggering event well in advance, and the possible presence of civil structures along the path of propagation (Iverson, 2003; Jenkins et al., 2017). Thus, the modelling of propagation of such flows and their interaction with structures is particularly relevant for risk management. It is of utmost importance to evaluate the forces acting on buildings and on structure in order to design different kinds of countermeasures, such as protective flexible and rigid barriers (Mizuyama, 2008; Ng et al., 2017; Scifoni et al., 2010). Both experiments and numerical simulations have been widely used for evaluating the impact dynamics of debris/mud/lava flows against rigid walls.

Considering dry granular and debris flows, many experimental research addressed the impact through field (e.g. Hu et al., 2011; Marchi et al., 2002) and laboratory (e.g. Armanini and Scotton, 1993; Cui et al., 2015) investigations. Small-scale laboratory experiments (Choi et al., 2015; Ng et al., 2021; Scheidl et al., 2013) permitted the systematic study of the complex flow-structure interaction under controlled conditions. These investigations allowed to define the peak value of the impact force and different simplified theoretical continuum-based approaches have been used to deduce semi-empirical formulas (e.g. Armanini, 2009; Armanini and Scotton, 1993; Bugnion et al., 2012; Vagnon and Segalini, 2016) based on different consideration and hypothesis.

The impact of a mud-flow against an obstacle has been experimentally analyzed by (Tiberghien et al., 2007). The fluid was a Carbopol solution with yield stress, and the dynamics of the impact has been deeply analyzed through the measure of the local velocities and of the pressure distribution on the obstacle.

* Corresponding author.
E-mail addresses: cristiana.dicristo@unina.it (C. Di Cristo), oreste.fecarotta@unina.it (O. Fecarotta), michele.iervolino@unicampania.it (M. Iervolino), vacca@unina.it (A. Vacca).

https://doi.org/10.1016/j.jhydrol.2022.128221
Received 12 January 2022; Received in revised form 15 June 2022; Accepted 12 July 2022
Available online 19 July 2022

Besides experimental investigations, numerical simulations based on appropriate flow models are nowadays commonly used to analyze the interaction of sediment-laden flows with obstacles.

For simulating debris/mud flows, both two-phase and one-phase models have been employed (Ancey, 2007; Coussot 2017a). The former approach, accounting for the mass and momentum equations for both the solid and fluid components, can independently reproduce the solid and fluid phase velocities (e.g., Di Cristo et al., 2016; Greco et al., 2012; Pudasaini, 2012) and has also been used to simulate the fluid structure interaction (e.g. Chiou et al., 2005; Di Cristo et al., 2020; Kattel et al., 2018). The one-phase models conversely consider the mixture as a homogeneous continuum with a non-Newtonian rheology either with a yield stress, such as Bingham (e.g. Imran et al., 2001; Liu and Mei, 1989; Liu and Mei 1989, Imran et al. 2001) and Herschel–Bulkley (e.g., Chanson et al., 2006; Coussot, 1994; Di Cristo et al., 2013; Huang and García, 1998; Maciel et al., 2017) models, or without it, i.e. the power-law model (e.g. Hwang et al., 1994; Ng and Mei, 1994). An extensive discussion concerning the role played by the yield stress may be found in Balmforth et al. (2014) and Coussot (2017b). Power-law rheological models are adequate to describe slurry matrices remaining essentially liquefied through the flow (Iverson, 2014), and they therefore may be used to reproduce the behavior of landslides (Carotenuto et al., 2015) and flows of natural estuarine muds (Bai and Tian, 2011; Zhang et al., 2010).

Simple one-phase models, despite the complexity due to degassing and cooling processes, can be usefully applied also to lava flows. Even if in some cases (high temperature and few gas) the lava can be efficiently modelled as either a Newtonian (e.g. Takagi and Huppert, 2010; Tallarico and Dragoni, 1999) or homogeneous non-Newtonian fluid. For example a Bingham rheology (Castruccio et al., 2013; Kelfoun and Vargas, 2016) can be adopted in the presence of bubbles and/or crystals and, depending on the amount of degassing that has occurred, both Herschel–Bulkley and power-law model (Tallarico et al., 2011; Balmforth and Craster, 2000; Conroy and Lev, 2021; Filippucci et al., 2010; Soule and Cashman, 2005) may be used to describe the fluid behaviour.

For these reasons, the one-phase model has been extensively used to investigate the interaction of both debris/mud (Ionescu, 2013; Rickenmann et al., 2006) and lava (Chirico et al., 2009; Fujita et al., 2009; Scifoni et al., 2010) waves with obstacles. However, to estimate the pressure/force caused by the impact of a wave against obstacles, one-phase models with yield stress have been mainly considered (Laigle et al., 2007; Tang et al., 2022; Wang et al., 2020; Zanuttigh and Lamberti, 2006) than the power-law model. The impact of a yield-less mud wave against obstacles has been numerically studied by Iervolino et al. (2017) and Greco et al. (2019). Both studies considered specific values of the rheological parameters, i.e. consistency ,μ_n, and power-law exponent, n, in order to represent the rheology of the catastrophic landslides occurred in 1999 in Cervinara (Italy) (Carotenuto et al., 2015).

Among the different proposals, the choice of the most suitable way to predict the impact force, and in particular its peak value, caused by a shear-thinning flow representative of a mud or a lava wave is still an open question. The present paper numerically analyzes the impact of a wave of shear-thinning power-law fluids against a rigid wall, systematically varying both the rheological parameters and flow conditions. Inspired by the fair accuracy of the depth-integrated schematization (Fent et al., 2018) in the estimation of the impact forces on rigid structures due to water (Aureli et al., 2015; Hien and Van Chien, 2021) and debris (Sarno et al., 2013; Zanuttigh and Lamberti, 2006) waves, the shallow-water model proposed by (Ng and Mei, 1994), valid when the length scale normal to the bottom is very small compared to longitudinal and transverse ones, has been herein considered. In details, this study analyzes the temporal history of the force, to evaluate its dependence on the values of the rheological parameters of the fluid (consistency, density and rheological index) and on the distance from the wall. The effect of the bed slope is also investigated. The results furnish useful indication for the evaluation of the peak force in different conditions.

The article is organized as follows. In Section 2 both the investigated problem and the governing equations are briefly described, while Section 3 reports the adopted numerical scheme and the performed tests. In Section 3 the results are presented and discussed; the conclusions are summarized in section 4.

2. Problem description and governing equations.

This study analyses the impact against a rigid wall of a mud-flow running over a steep slope, adopting the simple and idealized geometrical setting sketched in Fig. 1. A mass of mud, represented as an incompressible homogeneous shear-thinning power-law fluid, is instantaneously released and flows along a slope inclined of angle θ with respect the horizontal plane.

In the initial configuration the mud mass occupies a triangular wedge, with the depth $\widetilde{h}$ described by the following function:

$$\widetilde{h}(\widetilde{x},0) = \begin{cases} \widetilde{h}_o + \widetilde{x}tan\theta & -\widetilde{L}_u < \widetilde{x} < 0 \\ 0 & \widetilde{x} > 0 \end{cases}$$

with $\widetilde{x}$ the streamwise coordinate along the plane, $\widetilde{t}$ the time and $\widetilde{h}(\widetilde{x},\widetilde{t})$ the flow depth. The abscissa $\widetilde{x}=0$ corresponds to the downstream side of the triangle, $\widetilde{L}_u = \widetilde{h}_o\cot(\theta)$ is the length of the wedge for the given slope angle. A rigid wall, perpendicular to the bottom, is encountered downstream at distance $\widetilde{L}_d$ from the triangle side.

Considering a gradually-varied flow where spatial variations occur over scales larger than flow depth, a depth-averaged scheme is adopted. Flow resistance by the sidewalls is neglected with respect to that by the bottom. Considering the analogy with open channel clear-water flows, this simplification may be assumed whenever the width of the flow exceeds the depth by ten times or more (Chow, 2009).

Additionally, the surface tension is ignored and the mud rheology is decribed by the power-law model. The resulting flow model is represented by the following dimensional mass and momentum conservation equations (Di Cristo et al., 2014; Ng and Mei, 1994):

$$\frac{\partial \widetilde{h}}{\partial \widetilde{t}} + \frac{\partial \widetilde{q}}{\partial \widetilde{x}} = 0 \tag{1}$$

$$\frac{\partial \widetilde{q}}{\partial \widetilde{t}} + \beta_n \frac{\partial}{\partial \widetilde{x}}\left(\frac{\widetilde{q}^2}{\widetilde{h}}\right) + g\cos\theta \frac{\partial}{\partial \widetilde{x}}\frac{\widetilde{h}^2}{2} = g\widetilde{h}\sin\theta - \frac{\widetilde{\tau}_b}{\rho} \tag{2}$$

where $\widetilde{q}$ is the flow rate (for unit of width), g and ρ the gravity and the fluid density, respectively. β_n and $\widetilde{\tau}_b$ are the momentum correction factor and the bottom stress, respectively. Assuming laminar regime, the expressions of the momentum correction factor and of the bottom stress are:

$$\beta_n = 2\frac{2n+1}{3n+2} > 1 \tag{3}$$

$$\widetilde{\tau}_b = \mu_n\left(\frac{2n+1}{n}\frac{\widetilde{u}}{\widetilde{h}}\right)^n \tag{4}$$

respectively. In Eq. (3) and (4) $\widetilde{u} = \widetilde{q}/\widetilde{h}$ denotes the depth-averaged velocity; μ_n and n the consistency and the rheological index of the power-law fluid, respectively. The rheological index is smaller than one for shear-thinning fluids, while values larger than one pertains to shear-thickening ones. In the following, only shear-thinning fluids are considered. It is expected that the flow dynamics and the resulting impact force both depend on the geometry of the considered case, i.e. the inclination angle θ, the initial depth at the downstream side $\widetilde{h}_o$ and the wall distance $\widetilde{L}_d$, as well as on the rheological properties of the fluid, namely the density ρ, the consistency μ_n and the rheological index n.

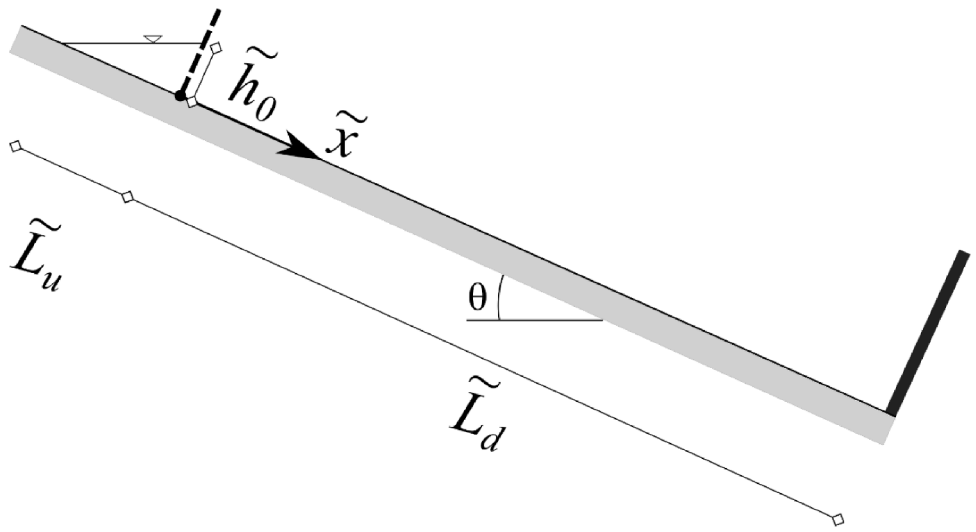

Fig. 1. Problem setup.

The problem is made dimensionless using $\tilde{L}_R = \tilde{h}_o$ and $\tilde{T}_R = \sqrt{\tilde{h}_o/g}$ as length and time scales, respectively. Denoting with h and $q = uh$ the dimensionless flow depth and flow rate, Eqs. (1)-(2) are rewritten in dimensionless form as:

$$\frac{\partial h}{\partial t} + \frac{\partial q}{\partial x} = 0 \tag{5}$$

$$\frac{\partial q}{\partial t} + \frac{\partial}{\partial x}\left(\beta_n \frac{q^2}{h}\right) + \cos\theta \frac{\partial}{\partial x}\left(\frac{h^2}{2}\right) = h\sin\theta - B_d \frac{q^n}{h^{2n}} \tag{6}$$

in which B_d, hereafter named Basal Drag coefficient, is expressed as:

$$B_d = \frac{\mu_n}{\rho}\left(\frac{2n+1}{n}\right)^n \sqrt{\frac{g^{n-2}}{\tilde{h}_o^{n+2}}} \tag{7}$$

Accounting for the length and time scales definitions, and the corresponding velocity scale, i.e. $\tilde{U}_R = \sqrt{g\tilde{h}_o}$, the Basal Drag coefficient can be expressed in terms of the reservoir Reynolds number Re (Chanson, 2008; Taha et al., 2018), written for a power-law fluid, as follows:

$$B_d = \left(\frac{2n+1}{n}\right)^n \frac{1}{Re} \quad with \quad Re = \frac{\rho \tilde{U}_R^{2-n} \tilde{L}_R^n}{\mu_n} \tag{8}$$

In a dam-break problem Re is the counterpart of the local Reynolds number (Ng and Mei, 1994).

In uniform condition, the flow may be assumed laminar provided that the local Reynolds number does not exceed the critical value (Ng and Mei 1994):

$$Re_c = 0.125\left(\frac{1+3n}{2n}\right)^n [2100 + 875(1-n)] \tag{9}$$

Assuming the validity in unsteady conditions of the bound (9) in terms of the reservoir Reynolds number, the flow may be considered laminar whenever the Basal Drag coefficient overwhelms the critical value:

$$B_{d,c} = \left(\frac{2n+1}{n}\right)^n \frac{1}{Re_c} \tag{10}$$

In addition to the values of n and B_d, the maximum value of impact force against the wall depends on the considered geometry, characterized by the inclination angle θ and the wall distance L_d.

3. Numerical method and performed tests

3.1. Numerical method

The non-linear hyperbolic system (5)-(6) has been numerically solved with a Finite Volume scheme which is second-order accurate in space and Total Variation Diminishing (TVD), and first-order accurate in time. In what follows the numerical scheme is briefly described.

Denoting the vector of the unknowns with $\boldsymbol{w} = [h, q]^T$, the governing Eqs. (5) and (6) are rewritten in following compact form:

$$\frac{\partial \boldsymbol{w}}{\partial t} + \frac{\partial \boldsymbol{f}(\boldsymbol{w})}{\partial x} = \boldsymbol{s}(\boldsymbol{w}) \tag{11}$$

in which the expressions of flux and source vectors, $\boldsymbol{f}$ and $\boldsymbol{s}$, directly follow from (5) and (6). Indicating with $\overline{\boldsymbol{w}}$ the average value of $\boldsymbol{w}$ in the finite volume of dimension Δx, with $\boldsymbol{f}^*$ the numerical approximation of the flux $\boldsymbol{f}$ at the interface between two volumes and $\boldsymbol{s}^*$ the volume-averaged value of the source term, the semi-discretized version of Eq. (11) is:

$$\frac{\partial \overline{\boldsymbol{w}}}{\partial t} + \frac{1}{\Delta x}\left(\boldsymbol{f}^*_{i+1/2} - \boldsymbol{f}^*_{i-1/2}\right) = \mathbf{s}^* \tag{12}$$

Following the Harten-Lax-Van Leer (HLL) scheme (Harten et al., 1983) and denoting with $\boldsymbol{w^L}$ (resp. $\boldsymbol{w^R}$) the $\boldsymbol{w}$ values on the left (resp. right) side of the interface, the following expression of numerical approximation of the flux has been considered:

$$\boldsymbol{f}^* = \frac{\lambda^R \mathrm{f}(\boldsymbol{w^L}) - \lambda^L \mathrm{f}(\boldsymbol{w^R}) + \lambda^R \lambda^L (\boldsymbol{w^R} - \boldsymbol{w^L})}{\lambda^R - \lambda^L} \tag{13}$$

Where:

$$\lambda^R = \max_{R,L}(\lambda^+, 0) \lambda^L = \min_{R,L}(\lambda^-, 0) \tag{14}$$

$\lambda^{\pm}$ being the slopes of the two characteristic lines of the system (11) and (12):

$$\lambda^{\pm} = \beta_n \frac{q}{h} \pm \sqrt{\beta_n(\beta_n - 1)\frac{q^2}{h^2} + h\cos\theta} \tag{15}$$

To guarantee the second-order spatial accuracy of the scheme, a piecewise linear reconstruction at the interfaces is performed to evaluate $\boldsymbol{w^L}$ and $\boldsymbol{w^R}$. Moreover, the non-linear minmod limiter (LeVeque, 2011) has been applied to preserve the solution monotonicity. Finally, the time discretization has been carried out through the first-order Euler method. The solid wall boundary condition at the end of the channel has been

implemented through the ghost cells technique (LeVeque, 2011).

The above numerical method possesses the typical simplicity, robustness, and built-in conservation properties of the Riemann solvers, which has led to many successful applications in shallow flow simulations involving highly discontinuous flows, transcritical flows, shock waves and moving wet–dry fronts. Among the approximate Riemann solvers, the adopted HLL scheme is often preferred in one-dimensional simulations since it does not require an iterative scheme, it is positive definite and generally computationally more efficient than other schemes. Additional details about the numerical scheme and the boundary conditions may be found in (Campomaggiore et al., 2016) and (Iervolino et al., 2017).

3.2. Validation of the numerical model reproducing an experimental dam break test

To demonstrate the capabilities of the considered flow model to simulate shallow flows of shear-thinning fluids, one of the dam-break experiments carried out by (Balmforth et al., 2007) has been reproduced. The experiment consists in the sudden release of a slump (2.2 cm height) of aqueous suspension of Xanthan gum with concentration order of 1 % in a 0.1 m wide, 0.6 m deep channel. The rheology of the considered shear-thinning fluid may be reasonably described by $n = 0.27$, $\mu_n = 6\text{Pa} \bullet \text{s}^n$, $\rho = 1000\text{kg} \bullet \text{m}^{-3}$. The fluid is kept at rest by a dam at $x = 0.4\text{m}$, which is rapidly lifted at $t = 0\text{s}$. The experiment has been simulated by considering $\Delta x = 0.005$ and $\Delta t = 0.004$. Fig. 2 compares the experimental measurements and the numerical reproduction of the downstream front position of the wave, denoted as x_f. The comparison shows that the computational model is able to reasonably reproduce the experimental results both in the near-field ($t \sim 0.2 \div 1$ s), where inertia plays a prominent role, and in the long-term one ($t \sim 100$ s), in which the fluid spreading is largely dominated by the bottom shear stress. For $t < 0.2$ s the agreement is less satisfactory, but, as noted by (Saramito et al., 2013), this short-term regime could be affected by the dam lifting more than by the flow inertia.

3.3. Performed tests of dam-break wave with impact

The numerical simulations of dam-break waves with impact (Fig. 1) have been carried out adopting spatial discretization step $\Delta x = 0.038$ and a temporal time step $\Delta t = 0.001$. Sensitivity to the discretization has been checked by halving the Δx and Δt under constant CFL, obtaining differences on the estimated peak force smaller than 1 %.

The performed tests investigate the influence on the dynamics and on the peak value of the impact force F (for unit width) due to the Basal Drag coefficient B_d, to the power-law exponent n and to the wall distance L_d for two values of the inclination angles, namely $\theta = 10^\circ$ ($L_u = 5.67$) and $\theta = 20^\circ$ ($L_u = 2.75$). With the aim of representing fluids with shear-thinning attitude, the power-law exponent has been varied between 0.2 and 0.9. Under these conditions, Basal Drag coefficient values of typical mud and lava flows range between 10^{-3} and 10^{-1}.

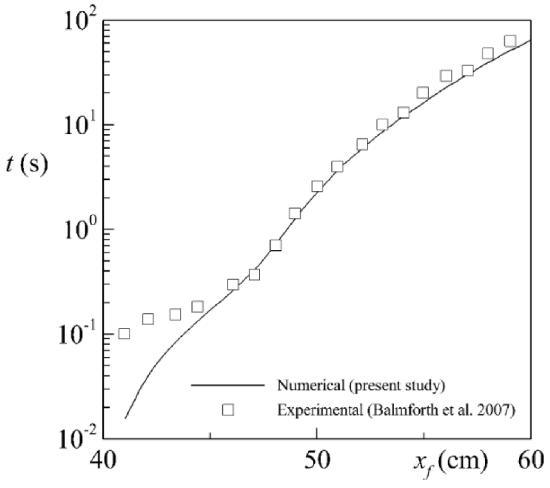

Fig. 2. Comparison between numerical (solid line) and experimental (symbols) of the downstream front position of the wave.

While the lower values of the above range of the Basal Drag coefficient may be encountered in both mud and lava flows, the higher ones may represent typical lava flows. This is exemplified in Table 1, where the Basal drag coefficient values for one mud and two different lava flows are reported. The considered mud (Case 1) is characterized by the following rheological parameters: $n = 0.14$, $\rho = 1440\text{Kg} \bullet \text{m}^{-3}$, $\mu_n = 104.1\text{Pa} \bullet \text{s}^n$ (Zhang et al., 2010). The other cases represent lava fluids with following rheology: Case 2 has $n = 0.763$, $\rho = 2780\text{Kg} \bullet \text{m}^{-3}$, $\mu_n = 51.88\text{Pa} \bullet \text{s}^n$ (Weed et al., 1986); Case 3 is characterized by $n = 0.9$, $\rho = 2650\text{Kg} \bullet \text{m}^{-3}$, $\mu_n = 1000\text{Pa} \bullet \text{s}^n$, (Filippucci et al., 2010). For these three fluids Table 1 reports the B_d values assuming an initial flow depth $\widetilde{h}_o = 1.8\text{m}$ and the critical Basal Drag values, $B_{d,c}$ (Eq.10), required to guarantee the occurrence of laminar condition. Results shown in Table 1 confirm that the flow can be safely considered laminar in all the herein studied cases.

Independently on the initial conditions and the governing parameters, the flow asymptotically in time approaches a quiescent condition with horizontal free surface. In this condition the impact force (for unit width) assumes the hydrostatic dimensionless value $F_{as} = 1/2$, which is used in what follows to normalize the instantaneous values of the impact force, $\widehat{F} = F/F_{as}$

4. Results and discussion

4.1. Impact dynamics

To assess the role of the Basal Drag coefficient B_d in the impact dynamics, Fig. 3 compares the time evolution of the normalised impact force $\widehat{F}$ for two different B_d values, namely $B_d = 10^{-3}$ and $B_d = 10^{-2}$, for a fluid with $n = 0.5$ and for a wall distance $L_d = 15$. The comparison is provided for $\theta = 20^\circ$ in Fig. 3a and for $\theta = 10^\circ$ in Fig. 3b.

Regardless of B_d and slope values, the force rapidly increases after the impact. For a given slope, the wave impact against the rigid wall occurs earlier for the smaller value of B_d. Soon after the front of the wave touches the obstacle, $\widehat{F}$ reaches a peak. Fig. 3a shows that at the lowest B_d value $\widehat{F}$ significantly grows over the asymptotic value, while in the $B_d = 10^{-2}$ case the F_{as} value is never overcome but only asymptotically reached. Moreover, for $B_d = 10^{-3}$, the peak is followed by a damped oscillatory trend, while in the $B_d = 10^{-2}$ case $\widehat{F}$ decreases after the peak and then it monotonically approaches the asymptotic value. Such a strong dependence of the force behaviour on the B_d coefficient essentially reflects the relative importance of the inertial and gravitational forces, along with the pressure gradient induced by the free surface, with respect to bottom resistance. Indeed, a smaller Basal Drag coefficient value corresponds to a reduced relevance of the bottom resistance, i.e., the second term at the r.h.s. of Eq.(6). This induces smaller momentum losses at the bottom and therefore higher values of the front velocity (v_f) and consequently of the peak force.

For the $\theta = 10^\circ$ case, Fig. 3b shows a similar temporal evolution of

Table 1
Basal drag coefficient.

	B_d	$B_{d,c}$
Case 1: (Zhang et al., 2010)	$6.3 \cdot 10^{-3}$	$3.1 \cdot 10^{-3}$
Case 2: (Weed et al., 1986)	$5.0 \cdot 10^{-3}$	$4.8 \cdot 10^{-3}$
Case 3: (Filippucci et al., 2010)	$1.3 \cdot 10^{-1}$	$5.3 \cdot 10^{-3}$

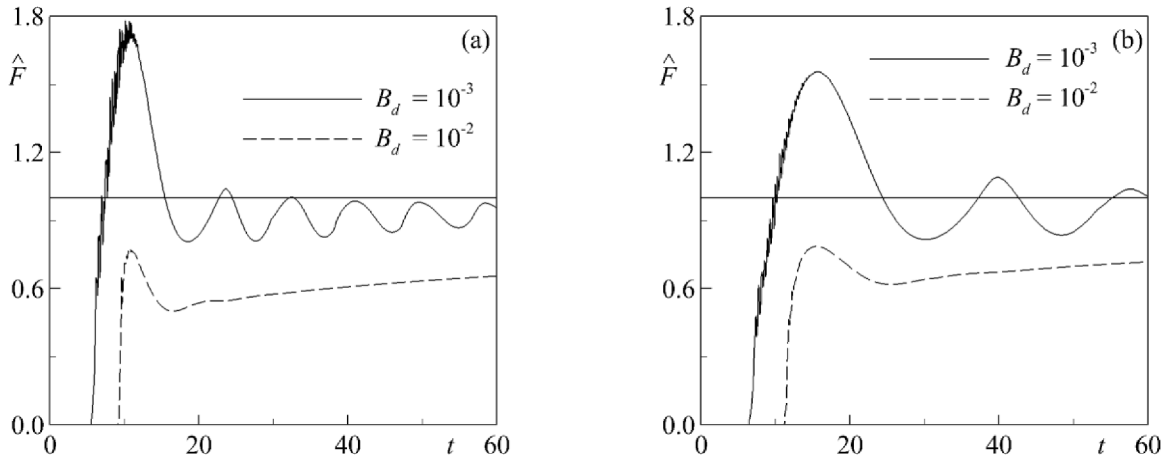

Fig. 3. Time evolution of the normalised impact force $\widehat{F}$ for two different B_d values, namely $B_d = 10^{-3}$ and $B_d = 10^{-2}$ (a) $\theta = 20°$; (b) $\theta = 10°$($n = 0.5, L_d = 15$).

the force, thus confirming the strong dependence of the front propagation velocity and of the peak force on the Basal Drag coefficient. Both front velocity propagation and peak force values in the $\theta = 10°$ case are smaller than the corresponding ones in the $\theta = 20°$ case.

The dependence of the impact force upon the power-law exponent can be inferred through the results presented in Fig. 4.

For fixed values of both Basal Drag coefficient ($B_d = 10^{-2}$) and the wall distance ($L_d = 15$), Fig. 4a and b report the time history of the normalized impact force $\widehat{F}$ for two different n values, namely $n = 0.2$ and $n = 0.9$, for the slope angles $\theta = 20°$ and $\theta = 10°$, respectively. Independently of the θ value, the reduction of the power-law exponent n induces an increase of the front velocity propagation (i.e. a reduction of wave impact time) and an increase of the force peak value.

The observed influence of the rheological index on the impact force behaviour (Fig. 4) can be explained considering that the power-law exponent plays a twofold role in the momentum conservation equation (Eq.6). Indeed, the power-law exponent influences both the bottom resistance, i.e. the second term at the r.h.s. of Eq. (6), and the convective inertia, i.e. the second term at the l.h.s. of Eq.6, through the momentum correction factor β_n (Eq.3). Since the front velocity (v_f) decreases with the bottom resistance and increases with the convective inertia, Hogg and Pritchard (2004) have shown that v_f can either increase with n (since the bottom resistance decreases with n) or decrease (since the convective inertia decreases for increasing n). Then, for sufficiently small B_d values the effect of the convective inertia prevails over the one due to the bottom resistance. Present results for $B_d = 10^{-2}$ agree with this theoretical interpretation, showing a reduction of the front propagation velocity with n. However, it is expected that higher B_d values could correspond to an opposite dependence of the front velocity with respect to the rheological exponent n. Fig. 5 reports the time evolution of the normalised impact force $\widehat{F}$ for $B_d = 0.05$ and three n values, for a wall distance L_d equals to 15.

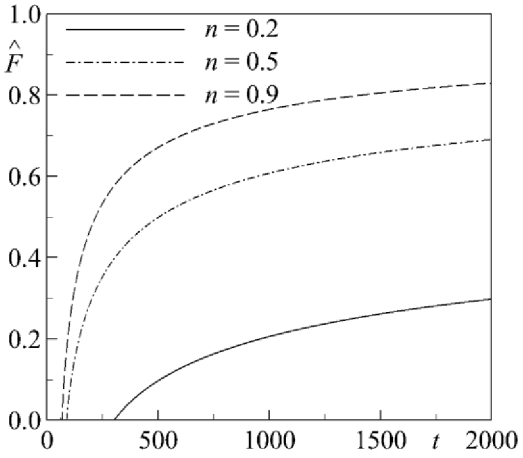

Fig. 5. Time evolution of the normalised impact force $\widehat{F}$ for $B_d = 0.05$ for three different n values, namely $n = 0.2, n = 0.5$ and.$n = 0.9$($L_d = 15, \theta = 20°$).

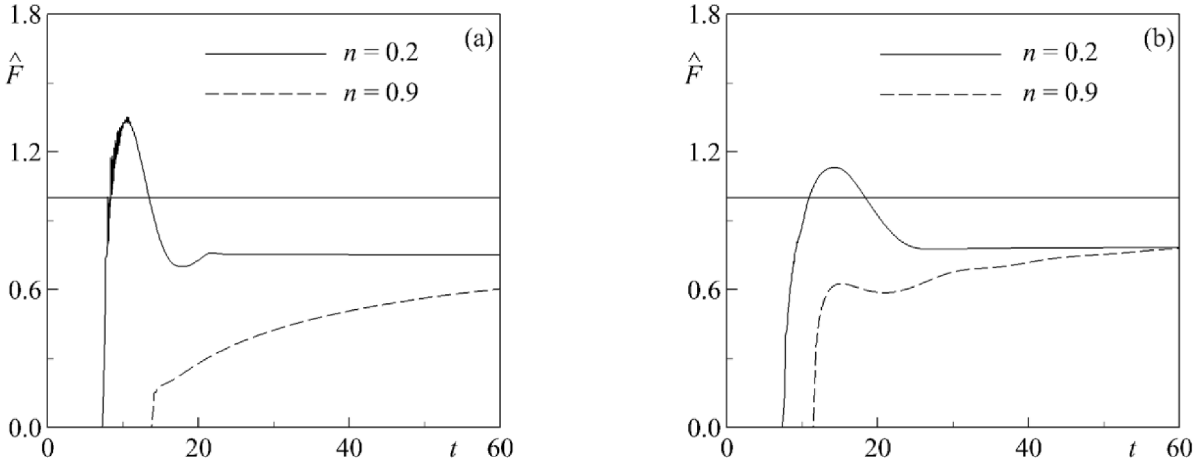

Fig. 4. Time evolution of the normalized impact force $\widehat{F}$ for two different n values, namely $n = 0.2$ and $n = 0.9$, (a) $\theta = 20°$; (b) $\theta = 10°$ ($B_d = 10^{-2}$; $L_d = 15$).

In this case, the increase of the Basal Drag coefficient is sufficient to revert the dependence of v_f, and therefore of force $\widehat{F}$, on n. As a result, the impact time is in this condition a decreasing function of the power-law exponent, witnessing that the effect of the bottom resistance prevails over the convective inertia.

Fig. 6 investigates the dependence of the impact force on the wall distance L_d. Considering $B_d = 10^{-2}$ and $n = 0.5$, Fig. 6a and b report the time history of the normalized impact force $\widehat{F}$ for $L_d = 5$ and $L_d = 20$, and considering again the two values of the slope for the tests $\theta = 20°$ and $\theta = 10°$. Independently of the θ value, Fig. 6 indicates that an increase of the wall distance reduces the maximum value of the impact force. Such a result is consistent with the increase of the momentum loss due to the bottom resistance forces with the distance travelled by the wave before the impact. As a result, depending on the wall distance the peak force may overwhelm or not the asymptotic hydrostatic value.

To further analyse the dependence of the impact force $\widehat{F}$ from the wall distance, Fig. 7 depicts the behaviour of the maximum force $\widehat{F}_{peak}$ as a function of L_d for three different n values, $B_d = 10^{-3}$ and $\theta = 20°$. Regardless the n value, Fig. 7 reveals a non-monotone behaviour of the peak force $\widehat{F}_{peak}$ with L_d, since $\widehat{F}_{peak}$ first increases, reaches a maximum and then decreases with L_d. This behaviour can be interpreted in the following way: while the gravity acts as a driving force increasing the momentum of the flow at the impact a short wall distance may not be sufficient to allow the resistance forces to produce an appreciable momentum loss. As the distance travelled by the wave increases, this trend reverts since the resistance prevails on the gravity and the peak force reduces with L_d. For sufficiently large L_d values, the resisting effect is so neat that the $\widehat{F}_{peak}$ reduces to 1, implying that the peak force is attained in the asymptotic hydrostatic condition.

4.2. Evaluation of the peak force

Previous results, taken collectively, indicate that, for a fixed value of the channel slope θ, the wave dynamics strongly depends on the (B_d, n, L_d) triplet. Consequently, the peak of the force against the obstacle may overwhelm the asymptotic value, i.e.: $\widehat{F}_{peak} > 1$, or not. In particular, Figs. 4 and 7 suggests that for a fixed slope a given pair (B_d, n), for wall distance longer than a minimum value, $L_{d,min}$, the condition $\widehat{F}_{peak} = 1$ is verified. For example, from Fig. 7 for $n = 0.5$ the minimum distance above which $\widehat{F}_{peak} = 1$ is 80.

Such a limiting value has been evaluated based on the results of numerous numerical simulations, for four values of the Basal Drag coefficient, i.e. $B_d = 10^{-3}, 2.5 \bullet 10^{-3}, 5.0 \bullet 10^{-3}, 10^{-2}$, and for values of the power-law exponent in the range $0.2 \leq n \leq 0.9$. The results are summarized in Fig. 8 for $\theta = 20°$ (Fig. 8a) and $\theta = 10°$ (Fig. 8b). Indeed, for a fixed value of B_d, in the portion of the (n, L_d) plane bounded on the left by the corresponding curve, the peak value of the force against the obstacle coincides with the asymptotic value, i.e.: $\widehat{F}_{peak} = 1$.

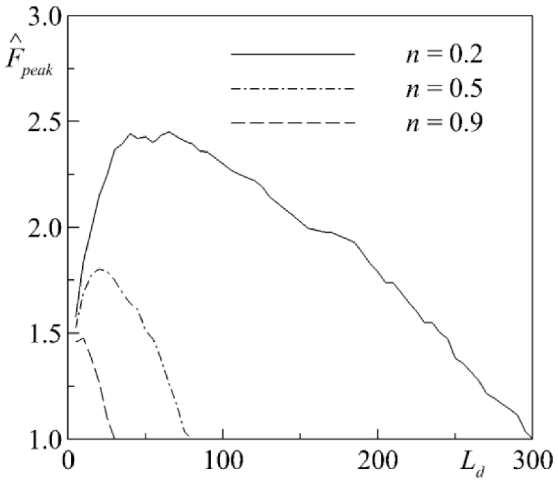

Fig. 7. Normalized peak force $\widehat{F}_{peak}$ as fuction of L_d for three different n values, namely $n = 0.2, n = 0.5$ and $n = 0.9 (B_d = 10^{-3}, \theta = 20°)$.

With reference to the largest considered slope value $\theta = 20°$, Fig. 8a shows that, keeping fixed the Basal Drag coefficient, an increase of the power-law exponent n leads to smaller values of $L_{d,min}$. Similar conclusions are drawn keeping fixed n and increasing B_d. Both results are consistent with the reduction of the front velocity due to an increase either of B_d (for a fixed value of n, see Fig. 3a) or of n (for a fixed value of B_d, see Fig. 4a). This trend is confirmed also in the $\theta = 10°$ case (Fig. 8b). For a fixed value of the (B_d, n) pair, the $L_{d,min}$ value in the $\theta = 10°$ case is smaller than in the $\theta = 20°$ one.

Fig. 8 furnishes the lower bound of the wall distance $L_{d,min}$ above which the force peak does not exceed its asymptotic value. Therefore, if only the maximum value of force against the obstacle is of interest, the asymptotic value $F_{as} = 1/2$ represents a safe assumption provided that the dimensionless wall distance exceeds $L_{d,min}$. Coherently with the results of Fig. 5, Fig. 8 shows that for a sufficiently high Basal Drag coefficient, i.e. $B_d > 10^{-2}$, the asymptotic value may be safely assumed, independently of the wall distance.

On the other hand, whenever the Basal Drag coefficient is smaller than 10^{-2} and the wall distance is smaller than $L_{d,min}$, the peak force exceeds the asymptotic value, and a detailed numerical simulation is required for its evaluation. To provide a comprehensive picture of the

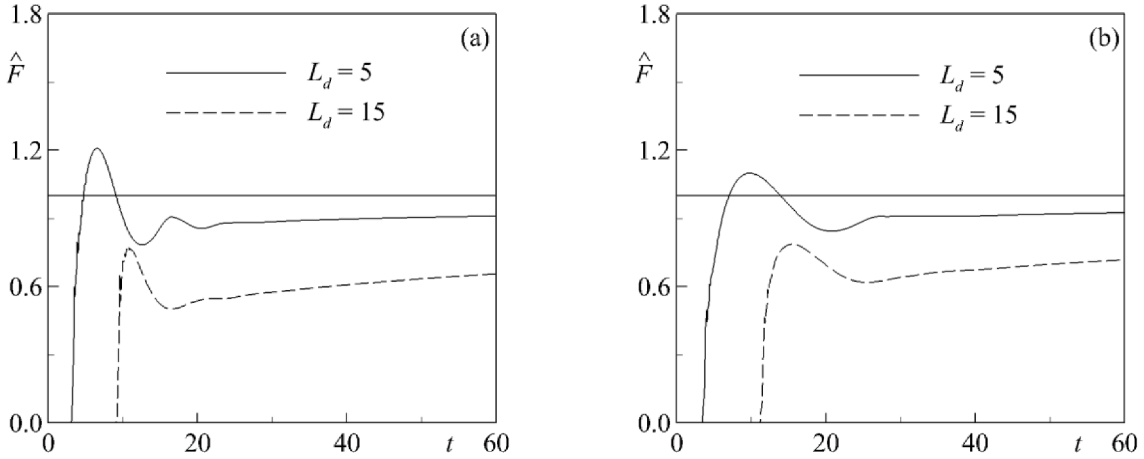

Fig. 6. Time evolution of the normalized impact force $\widehat{F}$ for two different $L_d$values, namely $L_d = 5$ and $L_d = 20$. (a) ; (b) $\theta = 10° (B_d = 10^{-2}; n = 5)$.

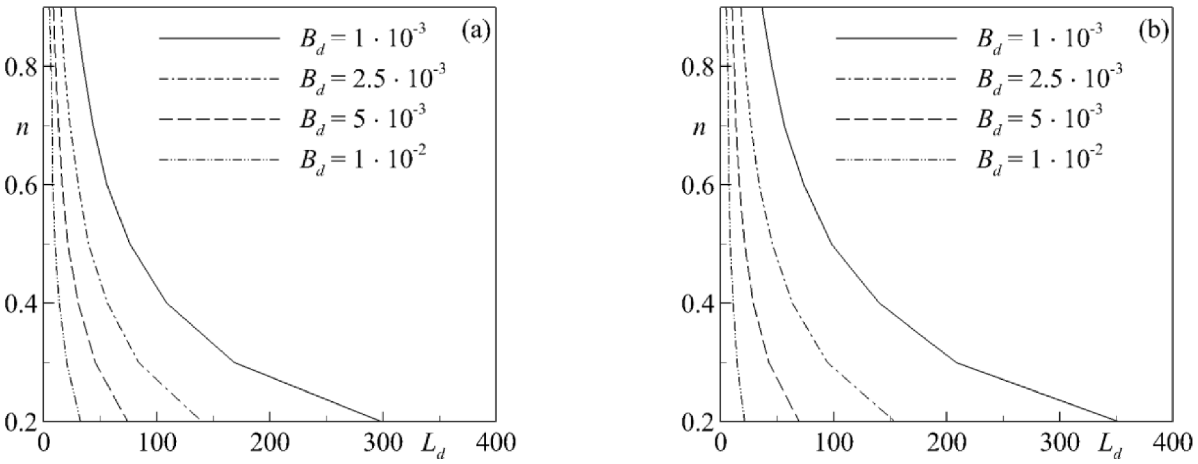

Fig. 8. Limit wall distance for different n and B_d values. (a) $\theta = 20°$; (b) $\theta = 10°$.

behaviour of the peak force value in these conditions, Figs. 9 and 10 report, for $L_d \leqslant L_{d,\min}$, the isolines of $\widehat{F}_{peak}$ in the (L_d, n) plane for $\theta = 20°$ and $\theta = 10°$, respectively, and considering four different Basal Drag values, i.e. $B_d = 10^{-3}, 2.5 \bullet 10^{-3}, 5.0 \bullet 10^{-3}$. For a fixed value of $\widehat{F}_{peak} = \widehat{F}^{*}_{peak}$, i.e. for a given curve reported in Figs. 9 and 10, the (B_d, n) pairs inside the region bounded on the right and/or on the top by the curve exhibit $\widehat{F}_{peak} \geq \widehat{F}^{*}_{peak}$.

For practical applications, Figs. 9 and 10 allow to quickly estimate

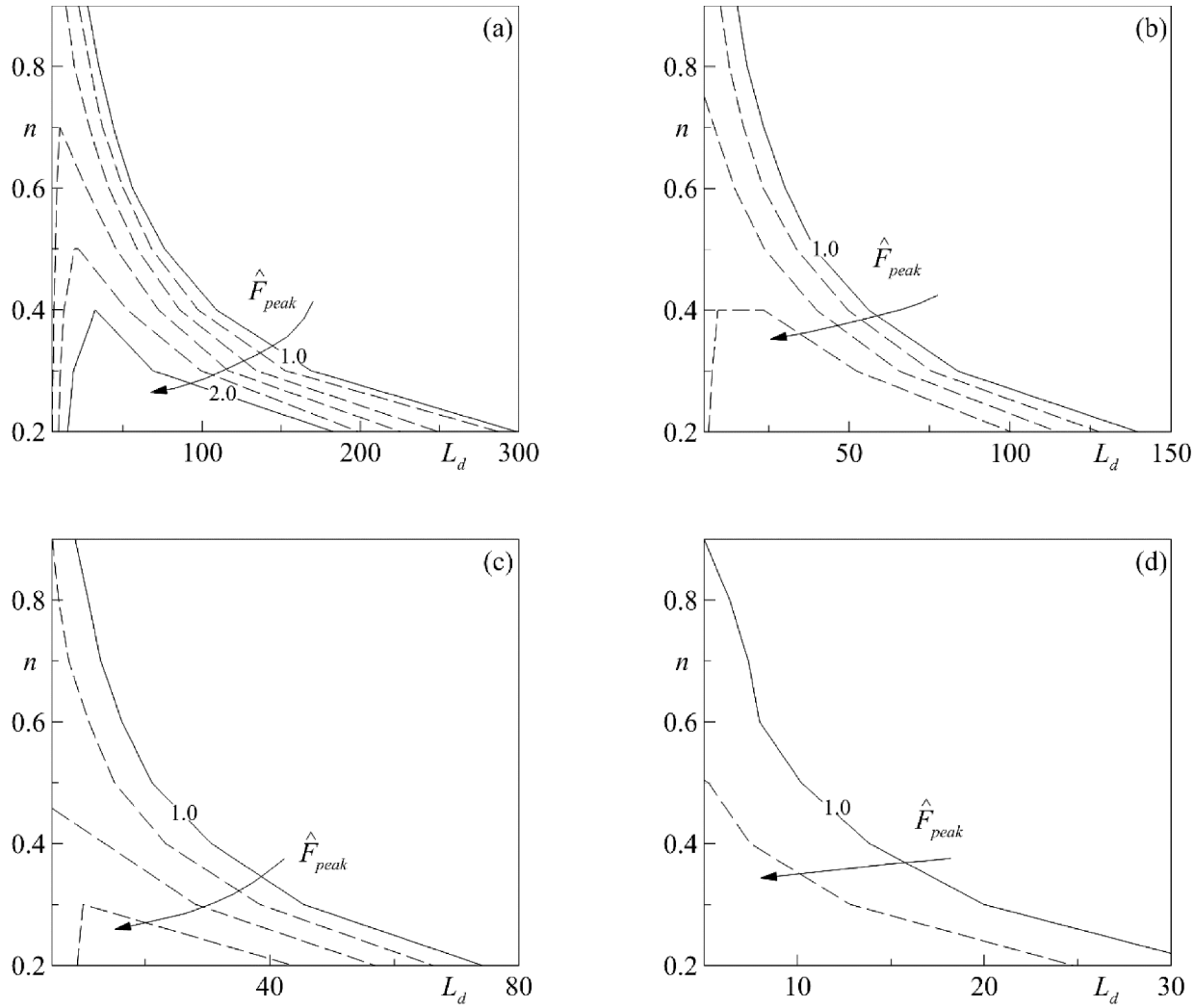

Fig. 9. Isocontours of $\widehat{F}_{peak}$ for $\theta = 20°$ in the (L_d, n) with spacing equal to 0.2. (a)$B_d = 10^{-3}$; (b) $B_d = 2.5 10^{-3}$; (c) $B_d = 5 10^{-3}$; (d)$B_d = 10^{-2}$.

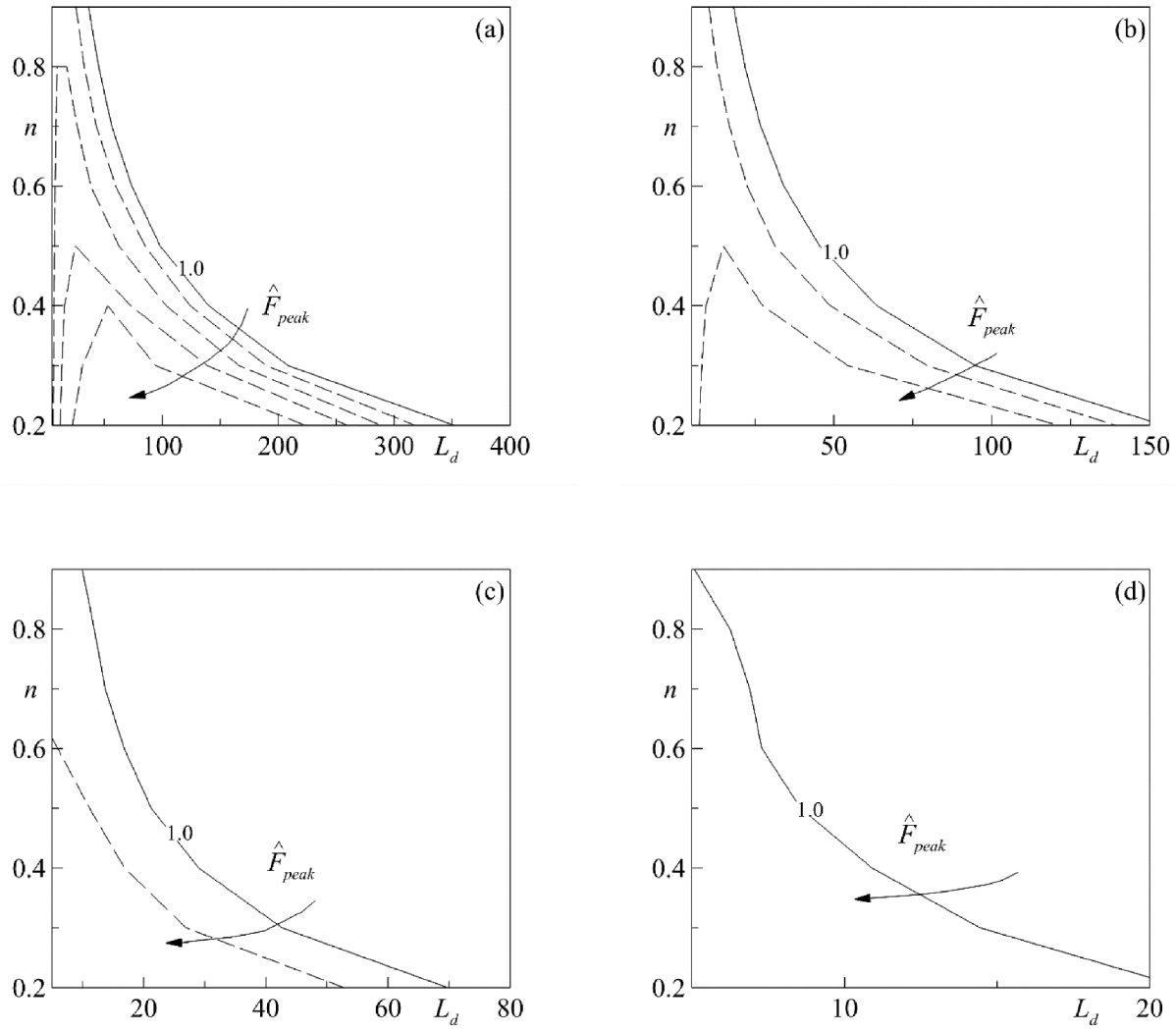

Fig. 10. Isocontours of $\widehat{F}_{peak}$ for $\theta = 10°$ in the (L_d, n) plane with spacing equal to 0.2. (a)$B_d = 10^{-3}$; (b) $B_d = 2.5 10^{-3}$; (c) $B_d = 5 10^{-3}$; (d) $B_d = 10^{-2}$.

for different fluids the amount by which the peak force exceeds the asymptotic value as function of the wall distance. The most demanding condition in the perspective of wall design occurs for $B_d = 10^{-3}$, for which Fig. 10a shows that $\widehat{F}^{*}_{peak}$ varies in the range 1.0–2.5. In a specific set of conditions, i.e. for fluid characterized by small value of the power-law exponent, $(n \leq 0.3)$ and for wall distance smaller than the values represented by the 2.0 curve, the peak force exceeds twice the asymptotic hydrostatic value. To pinpoint these most critical conditions for fluids with different rheological properties, Table 2 reports the maximum peak impact force for a given fluid rheology, $\widehat{F}_{max} = \max_{L_d}(\widehat{F}_{peak})$, and the corresponding wall distance $L_{d,max}$. The maximum value of the peak force strongly reduces with the Basal Drag coefficient. For example, for $n = 0.2$ and $B_d = 10^{-3}$ the maximum peak force equals 2.45, whereas this value reduces to 2.11, 1.73 and 1.40 for $B_d = 2.5 \bullet 10^{-3}$, $B_d = 5 \bullet 10^{-3}$, and $B_d = 10^{-2}$, respectively.

Fig. 10 shows that the above described behaviour does not change for the milder considered slope ($\theta = 10°$), although the force peak values are smaller than in the previous case. For example, even for $B_d = 10^{-3}$, Fig. 10a indicates that for $n = 0.3$ the peak value does not double the asymptotic value. Table 3 is the counterpart of Table 2 for the $\theta = 10°$

Table 2
Maximum peak impact force and the corresponding wall distance for $\theta = 20°$.

	$B_d = 10^{-3}$		$B_d = 2.5{\cdot}10^{-3}$		$B_d = 5{\cdot}10^{-3}$		$B_d = 10^{-2}$	
n	$L_{d,max}$	$\widehat{F}_{max}$	$L_{d,max}$	$\widehat{F}_{max}$	$L_{d,max}$	$\widehat{F}_{max}$	$L_{d,max}$	$\widehat{F}_{max}$
0.2	65	2.45	40	2.11	25	1.73	10	1.40
0.3	40	2.18	20	1.85	10	1.54	5	1.31
0.4	30	1.98	15	1.65	10	1.44	5	1.26
0.5	20	1.80	10	1.55	5	1.37	5	1.21
0.6	20	1.70	10	1.48	5	1.33	5	1.15
0.7	10	1.60	5	1.41	5	1.29	5	1.10
0.8	10	1.55	5	1.38	5	1.25	5	1.04
0.9	10	1.48	5	1.35	5	1.20	5	0.98

Table 3
Maximum peak impact force and the corresponding wall distance for $\theta = 20°$.

	$B_d = 10^{-3}$		$B_d = 2.5{\cdot}10^{-3}$		$B_d = 5{\cdot}10^{-3}$		$B_d = 10^{-2}$	
n	$L_{d,max}$	$\widehat{F}_{max}$	$L_{d,max}$	$\widehat{F}_{max}$	$L_{d,max}$	$\widehat{F}_{max}$	$L_{d,max}$	$\widehat{F}_{max}$
0.2	85	2.17	40	1.71	20	1.40	5	1.16
0.3	55	1.89	25	1.54	10	1.32	5	1.14
0.4	40	1.71	15	1.45	10	1.27	5	1.12
0.5	25	1.6	15	1.38	5	1.23	5	1.10
0.6	20	1.53	10	1.34	5	1.21	5	1.07
0.7	15	1.47	10	1.3	5	1.19	5	1.05
0.8	60	1.42	5	1.26	5	1.17	5	1.03
0.9	10	1.39	5	1.25	5	1.15	5	1.00

case. The maximum peak force $\widehat{F}_{max}$ equals 2.17 for $n = 0.2$ and $B_d = 10^{-3}$. This extreme value reduces increasing n and B_d, values, consistently with the results shown by Figs. 3b and 4b.

The contour plots of Figs. 9a, b, 10a and b show that, for certain values of n, increasing L_d the peak force firstly grows, then reaches a maximum and finally decreases. This behaviour is coherent with the results shown in Fig. 7, due to the combined effect of the flow acceleration and momentum losses.

In conclusion, the presented results suggest that the fluid rheology has a strong influence on the dynamic of the impact, as indicated by the different behaviour of the temporal evolution of the force observed for value of the Basal Drag smaller or larger than 10^{-2}. Moreover, in the condition $B_d \leq 10^{-2}$, the asymptotic hydrostatic value may be exceeded depending on the rheological index value and the wall distance. In particular, the rheological index strongly influences the peak force, which grows as n decreases. As far as the wall distance is concerned, it is possible to individuate a limit value, above which the maximum impact force corresponds to the final hydrostatic condition.

Whenever the sidewalls flow resistance cannot be neglected with respect to the bottom one, it may be conjectured that the application of present results would lead to a conservative estimation in terms of $\widehat{F}_{peak}$ and therefore in terms of $L_{d,min}$.

5. Conclusions

The present paper investigates the impact force against a rigid wall due to dam-break wave of a shear-thinning power-law fluid. A one-dimensional shallow water model is used, and a second-order Finite Volume scheme is employed to numerically solve the governing equations. Several numerical tests have been performed to investigate the influence on the dynamics and on the peak value of the impact force of the rheological characters of the fluids and of the problem geometry. In the performed tests the model parameters, Basal Drag coefficient B_d and power-law exponent n have been varied in realistic ranges for mud and lava flows and several dimensionless wall distance L_d have been considered for two values of the inclination angles, namely $\theta = 10^{\circ}$ and $\theta = 20^{\circ}$.

The results show that, for fixed values of the channel slope θ, the (B_d, n, L_d) values strongly influence the wave dynamics and two different behaviours of the temporal evolution have been found. Indeed, or the force sharply increases, and the peak value overwhelms the final hydrostatic value, or the force grows smoothly in time asymptotically approaching the hydrostatic value. For a fixed value of the power-law exponent, the latter behaviour occurs whenever the Basal Drag coefficient is sufficiently high and, in these cases, the asymptotic value may be safely assumed to evaluate the peak force. Conversely, for small Basal Drag the peak force may overwhelm the asymptotic value or not depending on L_d values. Indeed, there exists a minimum value of the wall distance $(L_{d,min})$ above which the peak force does not exceed its asymptotic hydrostatic value, i.e.: $\widehat{F}_{peak} = 1$. The minimum value of the wall distance $L_{d,min}$ has been found to strongly increase when the power-law exponent is reduced. For two different values of the channel slope, the dimensionless value of this lower bound, $L_{d,min,}$ is individuated considering several values of the dimensionless governing parameters (B_d, n). Moreover, for $L_d \leqslant L_{d,\min}$, an evaluation of the maximum value of the peak forces is also provided. The results of this work represent a novel contribution on the evaluation of the force produced by a mud/lava flow wave on a rigid obstacle, furnishing a theoretical interpretation of the impact dynamics and useful applicative indications on the estimation of the peak value.

CRediT authorship contribution statement

Cristiana Di Cristo: Conceptualization, Software, Writing – original draft, Writing – review & editing. **Oreste Fecarotta:** Software, Data curation, Writing – original draft, Writing – review & editing. **Michele Iervolino:** Software, Funding acquisition, Validation, Writing – original draft, Writing – review & editing. **Andrea Vacca:** Conceptualization, Software, Writing – original draft, Writing – review & editing.

Funding

M.I. contributed to this research within the SEND intra-university project, financed through the "V:ALERE 2019" program of the University of Campania "L. Vanvitelli" (Grant ID: B68D19001880005).

Declaration of Competing Interest

The authors declare that they have no known competing financial interests or personal relationships that could have appeared to influence the work reported in this paper.

Data availability

Data will be made available on request.

References

Ancey, C., 2007. Plasticity and geophysical flows: a review. J. Nonnewton. Fluid Mech. 142 (1–3), 4–35. https://doi.org/10.1016/j.jnnfm.2006.05.005.

Armanini, A., & Scotton, P. (1993). On the dynamic impact of a debris flow on structures. *Proceedings of XXV IAHR Congress*, 203–210.

Armanini, A. (2009). Discussion of 'Experimental analysis of the impact of dry avalanches on structure and implication for debris flows by B. Zanuttigh and A. Lamberti, Journal of Hydraulic Research, IAHR, 2006, 44(4), 522–534.' *Journal of Hydraulic Research*, *47*(3), 381–383. https://doi.org/10.1080/00221686.2009.9522009.

Aureli, F., Dazzi, S., Maranzoni, A., Mignosa, P., Vacondio, R., 2015. Experimental and numerical evaluation of the force due to the impact of a dam-break wave on a structure. Adv. Water Resour. 76, 29–42. https://doi.org/10.1016/j.advwatres.2014.11.009.

Bai, Y.C., Tian, Q., 2011. Interaction between mud and wave in different rheological models. J. Tianjin Univers. (Sci. Technol.) 44 (3), 196–201.

Balmforth, N.J., Craster, R.V., 2000. Dynamics of cooling domes of viscoplastic fluid. J. Fluid Mech. 422, 225–248. https://doi.org/10.1017/S002211200000166X.

Balmforth, N.J., Craster, R.V., Perona, P., Rust, A.C., Sassi, R., 2007. Viscoplastic dam breaks and the Bostwick consistometer. J. Nonnewton. Fluid Mech. 142 (1–3), 63–78. https://doi.org/10.1016/j.jnnfm.2006.06.005.

Balmforth, N.J., Frigaard, I.A., Ovarlez, G., 2014. Yielding to stress: recent developments in viscoplastic fluid mechanics. Annu. Rev. Fluid Mech. 46 (1), 121–146. https://doi.org/10.1146/annurev-fluid-010313-141424.

Bugnion, L., McArdell, B.W., Bartelt, P., Wendeler, C., 2012. Measurements of hillslope debris flow impact pressure on obstacles. Landslides 9 (2), 179–187. https://doi.org/10.1007/s10346-011-0294-4.

Campomaggiore, F., Di Cristo, C., Iervolino, M., Vacca, A., 2016. Development of roll-waves in power-law fluids with non-uniform initial conditions. J. Hydraul. Res. 54 (3), 289–306. https://doi.org/10.1080/00221686.2016.1140684.

Carotenuto, C., Merola, M.C., Álvarez-Romero, M., Coppola, E., Minale, M., 2015. Rheology of natural slurries involved in a rapid mudflow with different soil organic carbon content. Colloids Surf., A 466, 57–65. https://doi.org/10.1016/j.colsurfa.2014.10.037.

Castruccio, A., Rust, A.C., Sparks, R.S.J., 2013. Evolution of crust- and core-dominated lava flows using scaling analysis. Bull. Volcanol. 75 (1), 681. https://doi.org/10.1007/s00445-012-0681-2.

Chanson, H., 2008. A simple solution of the laminar dam break wave. J. Appl. Fluid Mech. 1 (1). https://doi.org/10.36884/jafm.1.01.11831.

Chanson, H., Jarny, S., Coussot, P., 2006. Dam break wave of thixotropic fluid. J. Hydraul. Eng. 132 (3), 280–293. https://doi.org/10.1061/(ASCE)0733-9429(2006)132:3(280).

Chiou, M.-C., Wang, Y., Hutter, K., 2005. Influence of obstacles on rapid granular flows. Acta Mech. 175 (1–4), 105–122. https://doi.org/10.1007/s00707-004-0208-9.

Chirico, G.D., Favalli, M., Papale, P., Boschi, E., Pareschi, M.T., Mamou-Mani, A., 2009. Lava flow hazard at nyiragongo volcano, DRC: 2. hazard reduction in urban areas. Bull. Volcanol. 71 (4), 375–387. https://doi.org/10.1007/s00445-008-0232-z.

Choi, C.E., Au-Yeung, S.C.H., Ng, C.W.W., Song, D., 2015. Flume investigation of landslide granular debris and water runup mechanisms. Géotech. Lett. 5 (1), 28–32. https://doi.org/10.1680/geolett.14.00080.

Chow, V. T. (2009). *Open-channel hydraulics*. Blackburn Press.

Conroy, C.J., Lev, E., 2021. A discontinuous Galerkin finite-element model for fast channelized lava flows v1.0. Geosci. Model Dev. 14 (6), 3553–3575. https://doi.org/10.5194/gmd-14-3553-2021.

Coussot, P., 1994. Steady, laminar, flow of concentrated mud suspensions in open channel. J. Hydraul. Res. 32 (4), 535–559. https://doi.org/10.1080/00221686.1994.9728354.
Coussot, P., 2017a. Mudflow Rheology and dynamics. Balkema, IAHR Monograph.
Coussot, P., 2017b. Bingham's heritage. Rheol. Acta 56 (3), 163–176. https://doi.org/10.1007/s00397-016-0983-y.
Cui, P., Zeng, C., Lei, Y., 2015. Experimental analysis on the impact force of viscous debris flow. Earth Surf. Proc. Land. 40 (12), 1644–1655. https://doi.org/10.1002/esp.3744.
Di Cristo, C., Greco, M., Iervolino, M., Leopardi, A., Vacca, A., 2013. Wave dynamics in a linearized mud-flow shallow model. Appl. Mathemat. Sci. 7 (5–8), 377–393.
Di Cristo, C., Iervolino, M., Vacca, A., 2014. Simplified wave models applicability to shallow mud flows modeled as power-law fluids. J. Mount. Sci. 11 (6), 1454–1465. https://doi.org/10.1007/s11629-014-3065-6.
Di Cristo, C., Greco, M., Iervolino, M., Leopardi, A., Vacca, A., 2016. Two-dimensional two-phase depth-integrated model for transients over mobile bed. J. Hydraul. Eng. 142 (2), 04015043. https://doi.org/10.1061/(ASCE)HY.1943-7900.0001024.
Di Cristo, C., Greco, M., Iervolino, M., Vacca, A., 2020. Interaction of a dam-break wave with an obstacle over an erodible floodplain. J. Hydroinf. 22 (1), 5–19. https://doi.org/10.2166/hydro.2019.014.
Fent, I., Putti, M., Gregoretti, C., Lanzoni, S., 2018. Modeling shallow water flows on general terrains. Adv. Water Resour. 121, 316–332. https://doi.org/10.1016/j.advwatres.2017.12.017.
Filippucci, M., Tallarico, A., Dragoni, M., 2010. A three-dimensional dynamical model for channeled lava flow with nonlinear rheology. J. Geophys. Res. 115 (B5), B05202. https://doi.org/10.1029/2009JB006335.
Fujita, E., Hidaka, M., Goto, A., Umino, S., 2009. Simulations of measures to control lava flows. Bull. Volcanol. 71 (4), 401–408. https://doi.org/10.1007/s00445-008-0229-7.
Greco, M., Iervolino, M., Leopardi, A., Vacca, A., 2012. A two-phase model for fast geomorphic shallow flows. Int. J. Sedim. Res. 27 (4), 409–425. https://doi.org/10.1016/S1001-6279(13)60001-3.
Greco, M., Di Cristo, C., Iervolino, M., Vacca, A., 2019. Numerical simulation of mud-flows impacting structures. J. Mount. Sci. 16 (2), 364–382. https://doi.org/10.1007/s11629-018-5279-5.
Harris, A.J.L., 2015. Basaltic Lava Flow Hazard. In: Volcanic Hazards, Risks and Disasters. Elsevier, pp. 17–46. https://doi.org/10.1016/B978-0-12-396453-3.00002-2.
Harten, A., Lax, P.D., van Leer, B., 1983. On upstream differencing and godunov-type schemes for hyperbolic conservation laws. SIAM Rev. 25 (1), 35–61. https://doi.org/10.1137/1025002.
Hien, L.T.T., Van Chien, N., 2021. Investigate Impact Force of Dam-Break Flow against Structures by Both 2D and 3D Numerical Simulations. Water 13 (3), 344. https://doi.org/10.3390/w13030344.
Hogg, A.J., Pritchard, D., 2004. The effects of hydraulic resistance on dam-break and other shallow inertial flows. J. Fluid Mech. 501, 179–212. https://doi.org/10.1017/S0022112003007468.
Hu, K., Wei, F., Li, Y., 2011. Real-time measurement and preliminary analysis of debris-flow impact force at Jiangjia Ravine, China: Real-Time Measurement and Analysis od Debris-Flow Impact Force. Earth Surf. Proc. Land. 36 (9), 1268–1278. https://doi.org/10.1002/esp.2155.
Huang, X., García, M.H., 1998. A herschel-bulkley model for mud flow down a slope. J. Fluid Mech. 374, 305–333. https://doi.org/10.1017/S0022112098002845.
Hwang, C.-C., Chen, J.-L., Wang, J.-S., Lin, J.-S., 1994. Linear stability of power law liquid film flows down an inclined plane. J. Phys. D Appl. Phys. 27 (11), 2297–2301. https://doi.org/10.1088/0022-3727/27/11/008.
Iervolino, M., Carotenuto, C., Gisonni, C., Minale, M., Vacca, A., 2017. Impact forces of a supercritical flow of a shear thinning slurry against an obstacle. In: Mikoš, M., Casagli, N., Yin, Y., Sassa, K. (Eds.), Advancing Culture of Living With Landslides. Springer International Publishing, pp. 391–398. https://doi.org/10.1007/978-3-319-53485-5_46.
Imran, J., Harff, P., Parker, G., 2001. A numerical model of submarine debris flow with graphical user interface. Comput. Geosci. 27 (6), 717–729. https://doi.org/10.1016/S0098-3004(00)00124-2.
Ionescu, I.R., 2013. Viscoplastic shallow flow equations with topography. J. Nonnewton. Fluid Mech. 193, 116–128. https://doi.org/10.1016/j.jnnfm.2012.09.009.
Iverson, R.M., 2003. Debris-flow rheology myth. In: Rickenmann & Chen, . (Ed.), Debris-flow Hazards Mitigation: Mechanics, Prediction and Assessment. Millpress, pp. 303–314.
Iverson, R.M., 2014. Debris flows: behaviour and hazard assessment. Geol. Today 30 (1), 15–20. https://doi.org/10.1111/gto.12037.
Jenkins, S.F., Day, S.J., Faria, B.V.E., Fonseca, J.F.B.D., 2017. Damage from lava flows: Insights from the 2014–2015 eruption of Fogo, Cape Verde. J. Appl. Volcanol. 6 (1), 6. https://doi.org/10.1186/s13617-017-0057-6.
Kattel, P., Kafle, J., Fischer, J.-T., Mergili, M., Tuladhar, B.M., Pudasaini, S.P., 2018. Interaction of two-phase debris flow with obstacles. Eng. Geol. 242, 197–217. https://doi.org/10.1016/j.enggeo.2018.05.023.
Kelfoun, K., Vargas, S.V., 2016. VolcFlow capabilities and potential development for the simulation of lava flows. Geol. Soc. Spec. Publ. 426 (1), 337–343. https://doi.org/10.1144/SP426.8.
Laigle, D., Lachamp, P., Naaim, M., 2007. SPH-based numerical investigation of mudflow and other complex fluid flow interactions with structures. Comput. Geosci. 11 (4), 297–306. https://doi.org/10.1007/s10596-007-9053-y.
LeVeque, R. J. (2011). *Finite volume methods for hyperbolic problems* (10 th printed). Cambridge Univ. Press.
Liu, K.F., Mei, C.C., 1989. Slow spreading of a sheet of Bingham fluid on an inclined plane. J. Fluid Mech. 207, 505–529. https://doi.org/10.1017/S0022112089002685.
Maciel, G.F., Ferreira, F.O., Cunha, E.F., Fiorot, G.H., 2017. Experimental apparatus for roll-wave measurements and comparison with a 1D mathematical model. J. Hydraul. Eng. 143 (11), 04017046. https://doi.org/10.1061/(ASCE)HY.1943-7900.0001366.
Marchi, L., Arattano, M., Deganutti, A.M., 2002. Ten years of debris-flow monitoring in the Moscardo Torrent (Italian Alps). Geomorphology 46 (1–2), 1–17. https://doi.org/10.1016/S0169-555X(01)00162-3.
Mizuyama, T., 2008. Structural countermeasures for debris flow disasters. Int. J. Erosion Control Eng. 1 (2), 38–43. https://doi.org/10.13101/ijece.1.38.
Ng, C.W.W., Song, D., Choi, C.E., Liu, L.H.D., Kwan, J.S.H., Koo, R.C.H., Pun, W.K., 2017. Impact mechanisms of granular and viscous flows on rigid and flexible barriers. Can. Geotech. J. 54 (2), 188–206. https://doi.org/10.1139/cgj-2016-0128.
Ng, C.W.W., Majeed, U., Choi, C.E., De Silva, W.A.R.K., 2021. New impact equation using barrier Froude number for the design of dual rigid barriers against debris flows. Landslides 18 (6), 2309–2321. https://doi.org/10.1007/s10346-021-01631-7.
Ng, C.-O., Mei, C.C., 1994. Roll waves on a shallow layer of mud modelled as a power-law fluid. J. Fluid Mech. 263, 151–184. https://doi.org/10.1017/S0022112094004064.
O'Brien, J., 2003. Reasonable assumptions in routing a dam break mudflow. Proc. Debris Flow Hazards Mitigat. Mech. Predict. Assess. 1, 683–693.
Pudasaini, S.P., 2012. A general two-phase debris flow model. J. Geophys. Res. Earth Surf. 117 (F3), n/a-n/a. https://doi.org/10.1029/2011JF002186.
Rickenmann, D., Laigle, D., McArdell, B.W., Hübl, J., 2006. Comparison of 2D debris-flow simulation models with field events. Comput. Geosci. 10 (2), 241–264. https://doi.org/10.1007/s10596-005-9021-3.
Saramito, P., Smutek, C., Cordonnier, B., 2013. Numerical modeling of shallow non-newtonian flows: part I. The 1D horizontal dam break problem revisited. Int. J. Numer. Anal. Model. Ser. B 4 (3), 283–298.
Sarno, L., Carravetta, A., Martino, R., Tai, Y.-C., 2013. Pressure coefficient in dam-break flows of dry granular matter. J. Hydraul. Eng. 139 (11), 1126–1133. https://doi.org/10.1061/(ASCE)HY.1943-7900.0000772.
Scheidl, C., Chiari, M., Kaitna, R., Müllegger, M., Krawtschuk, A., Zimmermann, T., Proske, D., 2013. Analysing debris-flow impact models, based on a small scale modelling approach. Surv. Geophys. 34 (1), 121–140. https://doi.org/10.1007/s10712-012-9199-6.
Scifoni, S., Coltelli, M., Marsella, M., Proietti, C., Napoleoni, Q., Vicari, A., Del Negro, C., 2010. Mitigation of lava flow invasion hazard through optimized barrier configuration aided by numerical simulation: the case of the 2001 Etna eruption. J. Volcanol. Geoth. Res. 192 (1–2), 16–26. https://doi.org/10.1016/j.jvolgeores.2010.02.002.
Soule, S.A., Cashman, K.V., 2005. Shear rate dependence of the pāhoehoe-to-'a'ā transition: Analog experiments. Geology 33 (5), 361. https://doi.org/10.1130/G21269.1.
Taha, T., Lateef, O.A.A., Pu, J.H., 2018. Laminar and turbulent analytical dam break wave modelling on dry-downstream open channel flow. Fluid Mech. Res. Int. J. 2 (5). https://doi.org/10.15406/fmrij.2018.02.00036.
Takagi, D., Huppert, H.E., 2010. Initial advance of long lava flows in open channels. J. Volcanol. Geoth. Res. 195 (2–4), 121–126. https://doi.org/10.1016/j.jvolgeores.2010.06.011.
Takahashi, T. (2018). *Debris flow: Mechanics, prediction and countermeasures* (2nd edition, first issued in paperback). CRC Press, a Balkema Book.
Tallarico, A., Dragoni, M., 1999. Viscous newtonian laminar flow in a rectangular channel: application to etna lava flows. Bull. Volcanol. 61 (1–2), 40–47. https://doi.org/10.1007/s004450050261.
Tallarico, A., Dragoni, A., Filippucci, M., Piombo, A., Santini, S., Valerio, A., 2011. Cooling of a channeled lava flow with non-newtonian rheology: crust formation and surface radiance. Ann. Geophys. 54 (5) https://doi.org/10.4401/ag-5335.
Tang, J., Lin, P., Cui, P., 2022. Depth-resolved numerical model of dam break mud flows with Herschel-Bulkley rheology. J. Mount. Sci. 19 (4), 1001–1017. https://doi.org/10.1007/s11629-021-7218-0.
Tiberghien, D., Laigle, D., Naaim, M., Thilbert, E., Ousset, F., 2007. In: Experimental Investigation of Interaction Between Mudflow and on Obstacle. Mechanics, Prediction and Assessment, Hazard Mitigation, pp. 281–292.
Vagnon, F., Segalini, A., 2016. Debris flow impact estimation on a rigid barrier. Nat. Hazards Earth Syst. Sci. 16 (7), 1691–1697. https://doi.org/10.5194/nhess-16-1691-2016.
Wang, Y., Liu, X., Yao, C., Li, Y., 2020. Debris-flow impact on piers with different cross-sectional shapes. J. Hydraul. Eng. 146 (1), 04019045. https://doi.org/10.1061/(ASCE)HY.1943-7900.0001656.
Weed, H.C., Ryerson, F.J., Piwinskii, A.J., 1986. Rheological properties of molten kilauea iki basalt containing suspended crystals. In: in Mineral Matter and Ash in Coal, pp. 223–233.
Widjaja, B., Hsien-Heng Lee, S., 2013. Flow box test for viscosity of soil in plastic and viscous liquid states. Soils Found. 53 (1), 35–46. https://doi.org/10.1016/j.sandf.2012.12.002.
Zanuttigh, B., Lamberti, A., 2006. Experimental analysis of the impact of dry avalanches on structures and implication for debris flows. J. Hydraul. Res. 44 (4), 522–534. https://doi.org/10.1080/00221686.2006.9521703.
Zhang, X., Bai, Y., Ng, C.O., 2010. Rheological properties of some marine muds dredged from china coasts. In: Proceedings of the 28 International Offshore and Polar Engineering Conference, pp. 455–461.